

# Measurement of the Antineutrino Spectrum from $^{235}\text{U}$ Fission at HFIR with PROSPECT

J. Ashenfelter,<sup>16</sup> A. B. Balantekin,<sup>14</sup> H. R. Band,<sup>16</sup> C. D. Bass,<sup>6</sup> D. E. Bergeron,<sup>7</sup> D. Berish,<sup>10</sup> N. S. Bowden,<sup>5</sup> J. P. Brodsky,<sup>5</sup> C. D. Bryan,<sup>8</sup> J. J. Cherwinka,<sup>14</sup> T. Classen,<sup>5</sup> A. J. Conant,<sup>3</sup> A. A. Cox,<sup>12</sup> D. Davee,<sup>15</sup> D. Dean,<sup>9</sup> G. Deichert,<sup>8</sup> M. V. Diwan,<sup>1</sup> M. J. Dolinski,<sup>2</sup> A. Erickson,<sup>3</sup> M. Febbraro,<sup>9</sup> B. T. Foust,<sup>16</sup> J. K. Gaison,<sup>16</sup> A. Galindo-Uribarri,<sup>9,11</sup> C. E. Gilbert,<sup>9,11</sup> K. E. Gilje,<sup>4</sup> B. T. Hackett,<sup>9,11</sup> S. Hans,<sup>1,\*</sup> A. B. Hansell,<sup>10</sup> K. M. Heeger,<sup>16</sup> J. Insler,<sup>2</sup> D. E. Jaffe,<sup>1</sup> X. Ji,<sup>1</sup> D. C. Jones,<sup>10</sup> O. Kyzlyova,<sup>2</sup> C. E. Lane,<sup>2</sup> T. J. Langford,<sup>16,†</sup> J. LaRosa,<sup>7</sup> B. R. Littlejohn,<sup>4</sup> X. Lu,<sup>9,11</sup> D. A. Martinez Caicedo,<sup>4</sup> J. T. Matta,<sup>9</sup> R. D. McKeown,<sup>15</sup> M. P. Mendenhall,<sup>5</sup> J. M. Minock,<sup>2</sup> P. E. Mueller,<sup>9</sup> H. P. Mumm,<sup>7</sup> J. Napolitano,<sup>10</sup> R. Neilson,<sup>2</sup> J. A. Nikkel,<sup>16</sup> D. Norcini,<sup>16</sup> S. Nour,<sup>7</sup> D. A. Pushin,<sup>12</sup> X. Qian,<sup>1</sup> E. Romero-Romero,<sup>9,11</sup> R. Rosero,<sup>1</sup> D. Sarenac,<sup>12</sup> P. T. Surukuchi,<sup>4</sup> A. B. Telles,<sup>16</sup> M. A. Tyra,<sup>7</sup> R. L. Varner,<sup>9</sup> B. Viren,<sup>1</sup> C. White,<sup>4</sup> J. Wilhelmi,<sup>10</sup> T. Wise,<sup>16</sup> M. Yeh,<sup>1</sup> Y.-R. Yen,<sup>2</sup> A. Zhang,<sup>1</sup> C. Zhang,<sup>1</sup> and X. Zhang<sup>4</sup>

(The PROSPECT Collaboration)<sup>‡</sup>

<sup>1</sup>Brookhaven National Laboratory, Upton, NY, USA

<sup>2</sup>Department of Physics, Drexel University, Philadelphia, PA, USA

<sup>3</sup>George W. Woodruff School of Mechanical Engineering, Georgia Institute of Technology, Atlanta, GA USA

<sup>4</sup>Department of Physics, Illinois Institute of Technology, Chicago, IL, USA

<sup>5</sup>Nuclear and Chemical Sciences Division, Lawrence Livermore National Laboratory, Livermore, CA, USA

<sup>6</sup>Department of Physics, Le Moyne College, Syracuse, NY, USA

<sup>7</sup>National Institute of Standards and Technology, Gaithersburg, MD, USA

<sup>8</sup>High Flux Isotope Reactor, Oak Ridge National Laboratory, Oak Ridge, TN, USA

<sup>9</sup>Physics Division, Oak Ridge National Laboratory, Oak Ridge, TN, USA

<sup>10</sup>Department of Physics, Temple University, Philadelphia, PA, USA

<sup>11</sup>Department of Physics and Astronomy, University of Tennessee, Knoxville, TN, USA

<sup>12</sup>Institute for Quantum Computing and Department of Physics and Astronomy, University of Waterloo, Waterloo, ON, Canada

<sup>13</sup>Department of Physics, University of Wisconsin, Madison, WI, USA

<sup>14</sup>Physical Sciences Laboratory, University of Wisconsin, Madison, WI, USA

<sup>15</sup>Department of Physics, College of William and Mary, Williamsburg, VA, USA

<sup>16</sup>Wright Laboratory, Department of Physics, Yale University, New Haven, CT, USA

(Dated: May 27, 2022)

This Letter reports the first measurement of the  $^{235}\text{U}$  antineutrino energy spectrum by PROSPECT, the Precision Reactor Oscillation and Spectrum experiment, operating 7.9 m from the 85 MW<sub>th</sub> highly-enriched uranium (HEU) High Flux Isotope Reactor. With an exposure of 3426 MW-days, PROSPECT has detected  $31678 \pm 304$  (stat.)  $\bar{\nu}_e$ -induced inverse beta decays, the largest sample from HEU fission to date, 99% of which are attributed to  $^{235}\text{U}$ . When compared to model predictions, PROSPECT disfavors  $^{235}\text{U}$  as the sole source of the  $\bar{\nu}_e$  energy spectrum discrepancy observed at nuclear power reactors at  $\sim 3\sigma$  C.L.

Reactor antineutrino experiments have been central to our understanding of neutrinos, including the first observation of antineutrinos [1], the discovery of  $\bar{\nu}_e$  oscillations [2], observation of  $\bar{\nu}_e$  produced within the Earth [3], and the measurement of the neutrino mixing angle  $\theta_{13}$  [4–6]. Nearly all of these experiments were located at low-enriched uranium (LEU) nuclear power reactors where more than 99% of emitted  $\bar{\nu}_e$  come from the beta decay of fission products of four isotopes ( $^{235}\text{U}$ ,  $^{238}\text{U}$ ,  $^{239}\text{Pu}$ , and  $^{241}\text{Pu}$ ). At power reactors, the emitted antineutrino flux and spectrum evolve over time as the isotopic composition changes in the fuel cycle. Comparisons between leading theoretical predictions and experimental results reveal a  $\sim 6\%$  global flux deficit [7, 8], disagreement of the energy spectrum [9–12], and isotopic-evolution [13, 14]. Explanations for these possibly independent phenomena may lie in the complex nuclear physics of reactors [15–22], physics beyond the Standard Model such as eV-scale sterile neutrinos [23], or both [24]. New experiments at compact-core highly enriched uranium (HEU) research reactors enable short baseline searches for sterile neutrino oscillations and the measurement

of the nearly time-independent emission of  $\bar{\nu}_e$  from  $^{235}\text{U}$  fission [25–27]. PROSPECT has recently reported a search for sterile neutrinos at the High Flux Isotope Reactor (HFIR) [28]. This Letter reports the first measurement of the  $\bar{\nu}_e$  energy spectrum from HFIR by the PROSPECT experiment.

Located at Oak Ridge National Laboratory, HFIR is an 85 megawatt thermal (MW<sub>th</sub>) HEU research reactor. The cylindrical reactor core (diameter: 0.435 m, height: 0.508 m) contains 93%  $^{235}\text{U}$  enriched fuel, leading to a  $>99\%$   $^{235}\text{U}$  fission fraction. Each 24-day operating cycle uses fresh fuel, minimizing production of  $^{239}\text{Pu}$  or  $^{241}\text{Pu}$ . Using 40.3 days of reactor-on and 37.8 days of reactor-off data, a total of  $31678 \pm 304$  (stat.)  $\bar{\nu}_e$  candidates were identified with measured energies between 0.8–7.2 MeV. This is the highest-statistics  $^{235}\text{U}$  spectral measurement since the ILL experiment observed  $\sim 5000$   $\bar{\nu}_e$  candidates in 1981 [29].

The PROSPECT detector [27] is deployed in a ground-level room at a center-to-center distance of  $7.9 \pm 0.1$  m from the reactor core. From this position, the core center is located  $40^\circ$  below the horizontal and the surrounding build-

ing provides less than one meter-water-equivalent of concrete overburden. PROSPECT uses inverse beta decay (IBD),  $\bar{\nu}_e + p \rightarrow \beta^+ + n$ , to detect  $\bar{\nu}_e$  within a 4-ton  ${}^6\text{Li}$ -loaded liquid scintillator ( ${}^6\text{LiLS}$ ) target divided into an  $11 \times 14$  array of optically isolated rectangular segments. The measured energy of  $\beta^+$  ionization and annihilation, or prompt signal, carries the  $\bar{\nu}_e$  energy information. The delayed neutrons principally capture on  ${}^6\text{Li}$  with an average time separation of  $\sim 50 \mu\text{s}$ . This prompt-delay coincident pair identifies IBD-like events. Each segment measures  $14.5 \text{ cm} \times 14.5 \text{ cm} \times 117.6 \text{ cm}$ , read out on both ends by  $12.7 \text{ cm}$  photomultiplier tubes (PMTs) [28]. Segments are rotated by  $5^\circ$  to create space for hollow plastic support rods at each corner, allowing radioactive sources and optical calibration inserts to be deployed adjacent to all fiducial segments.

Waveform digitizers (WFDs, 250 MHz, 14-bit) record signals generated by scintillation light collected by PMTs. The triggering scheme balances overall throughput with the need to capture small energy depositions from Compton scattering of  $511 \text{ keV}$  annihilation  $\gamma$ -rays. Observation of coincident signals in the two PMTs of any segment (combining to  $\sim 150 \text{ keV}$  deposition threshold) triggers waveform acquisition of all WFD channels. Any PMT signal that exceeds a zero-suppression threshold of  $\sim 2$  photoelectrons (PE) is stored for offline analysis. Individual pulses are integrated to determine the amount of light observed by each PMT. The time-separation and charge-ratio of the two PMT signals from each segment are combined to determine the interaction position ( $z$ ) along the segment length. The segment energy deposition is determined from a position-corrected PE count. The relative energy scale of each segment is determined from fitting the nLi capture peak. Depositions which occur within  $\sim 20 \text{ ns}$  are summed to produce the total reconstructed event energy ( $E_{rec}$ ). Variations in hardware digitization thresholds and light collection along segments are controlled by the application of a segment-wise  $85 \text{ keV}$  analysis threshold that results in uniform event acceptance across the entire detector volume. A metric for particle identification, Pulse Shape Discrimination (PSD), is determined from the ratio of the PMT pulse tail to the total pulse integral, effectively separating interactions from heavy and light charged particles. Further information on the detector design and data acquisition are given in Ref. [27].

The measured response from deployed and environmental radioactive calibration sources are used to constrain the PROSPECT GEANT4-based [30] Monte Carlo model (PG4). The spectra from cosmogenic  ${}^{12}\text{B}$  electrons (between [3, 13.4] MeV), neutron-hydrogen capture  $\gamma$ -rays, and centrally-deployed  $\gamma$ -ray sources ( ${}^{137}\text{Cs}$ ,  ${}^{60}\text{Co}$ , and  ${}^{22}\text{Na}$ ) are simultaneously fit to the PG4 detector response to determine the  $E_{rec}$  scale, nonlinearity, and resolution summed over all detector segments (Fig. 1). The segment multiplicity distributions from each calibration source are used as inputs to the fitting procedure. The multiplicity distribution of  ${}^{22}\text{Na}$  events closely resembles the topology of IBD positrons (both contain a main interaction accompanied by annihilation  $\gamma$ -rays) and

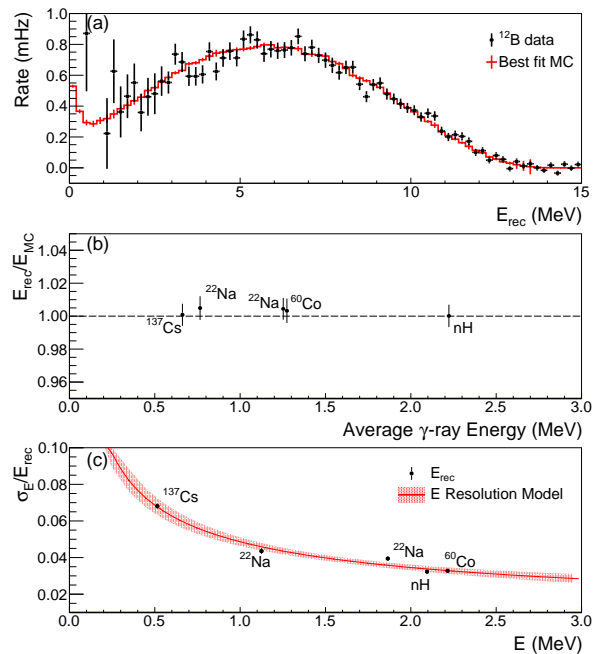


FIG. 1. (a): Measured  ${}^{12}\text{B}$  electron energy spectrum compared to the best-fit MC model. (b): Ratio of measured to simulated  $E_{rec}$  versus average  $\gamma$ -ray energy, showing a consistency of  $\pm 1\%$ . (c): Energy resolution of the full detector based on different calibration sources.

is shown in Fig. 2. The mean multiplicity of  ${}^{22}\text{Na}$  events is  $4.532 \pm 0.002$  compared to the best-fit MC mean multiplicity of  $4.535 \pm 0.002$ . Nonlinear scintillator response at low energies is parameterized using a combined Birks and Cherenkov model [31], and a photo-statistics dominated energy resolution of 4.8% is observed at 1 MeV.

As described in [28], a wide range of observables are used to track detector response stability and uniformity. For the data taking period considered here,  $E_{rec}$  and energy resolutions are stable to within  $\sim 1\%$  and  $\sim 10\%$ , respectively, and  $z$ -position and  $z$ -resolution are stable to 5 cm and  $\sim 10\%$ , over all times and segments. Small differences between segments and variations in time are unified through the addition of event-level smearing resulting in a 5% energy resolution at 1 MeV for all segments.

A detector response matrix is constructed by generating narrow bands, 50 keV wide, of  $\bar{\nu}_e$  energies spanning 1.8 to 10 MeV in PG4 and recording their separate  $E_{rec}$  spectra. One of these simulated  $E_{rec}$  spectra ([4.0, 4.05] MeV  $\bar{\nu}_e$ ) is shown in Fig. 2. A broadening of the main peak is observed from escaping annihilation  $\gamma$ -rays. Events with low prompt energy ( $\sim 0.5 \text{ MeV}$ ) are observed from IBD interactions which originate in inactive material but whose annihilation  $\gamma$ -rays and neutrons are detected in the active volume. The response matrix is used to convert from  $\bar{\nu}_e$  energy to the experimental prompt energy space [32].

During the data collection period considered here, a number of the PROSPECT PMTs displayed current instabilities. These PMTs were powered down and a total of 33 segments

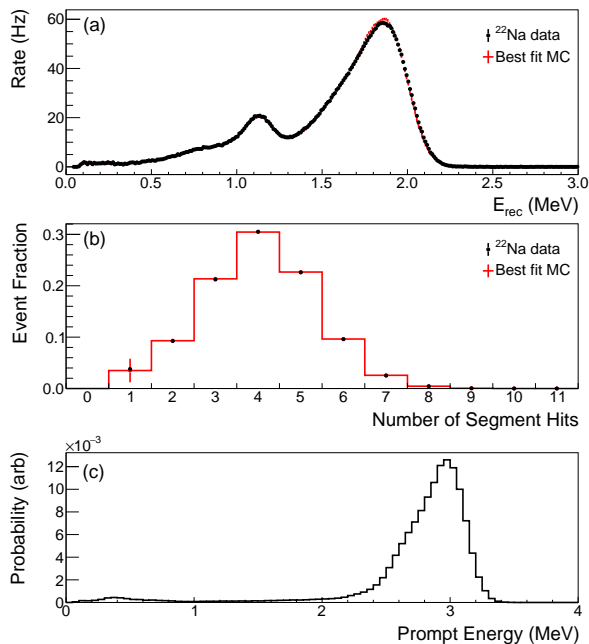


FIG. 2. (a): The measured and best-fit MC simulated  $^{22}\text{Na}$  spectra. (b) Distribution of segment multiplicity for simulated and measured  $^{22}\text{Na}$  data. (c) The simulated detector response to a narrow band of  $[4.0, 4.05]$  MeV  $\bar{\nu}_e$  energies. The main peak is asymmetrically broadened by escaping annihilation  $\gamma$ -rays.

have been excluded from the analysis. This has two main impacts on the analysis. First, disabled segments slightly reduce the efficiency of neighboring segments by lowering the acceptance of neutron captures outside of the primary interaction segment. Second, the increase in inactive material in the fiducial volume leads to an enhanced number of events with missing energy from escaping annihilation  $\gamma$ -rays. The disabled segments are included in the PG4 model to ensure that the detector response matrix accurately captures this effect.

The selection criteria to identify IBD candidates based on the prompt positron signal and a time- and position-correlated delayed signal from neutron capture on  $^6\text{Li}$  are similar to that described in Ref. [28]. A time-separation selection of  $(1, 120)$   $\mu\text{s}$  and position separation cut of  $\sim 15$  cm further reduce accidental coincidences. Prompt and delayed events with reconstructed positions in an outermost veto layer (1 segment width top and sides, two segment width bottom,  $>44.8$  cm from segment center) are rejected to reduce backgrounds from cosmogenic showers and  $\gamma$ -rays from experimental activity below the detector. IBD candidates that occur within 200  $\mu\text{s}$  after a muon interaction are vetoed to suppress multiple neutron capture events. Additionally, candidates that occur within a  $(-250, 250)$   $\mu\text{s}$  window of a neutron capture or nuclear recoil with  $E_{rec} > 0.25$  MeV are rejected. Selection criteria are based on measured segment-wise PSD performance to minimize bias between segments. Veto dead time fractions range from 11% to 14% due to time-varying  $\gamma$ -ray backgrounds that enter the nuclear recoil band.

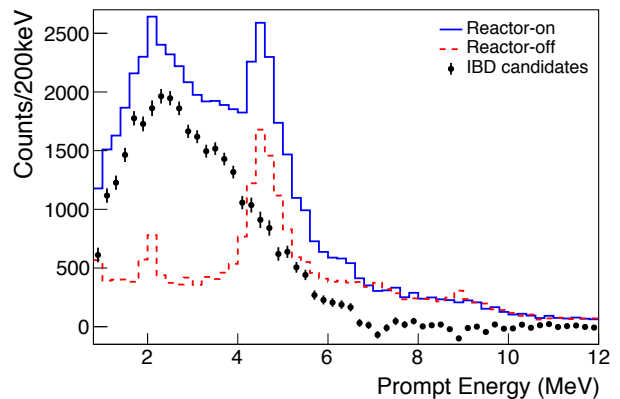


FIG. 3. The measured prompt energy spectrum of inverse beta decay events (with statistical errors only) compared to reactor-on and reactor-off correlated candidates. The reactor-off correlated candidates have been scaled to match the reactor-on exposure.

IBD candidate events with prompt  $E_{rec}$  from 0.8 MeV to 7.2 MeV are considered. The 40.3 (37.8) exposure-day reactor-on (reactor-off) data set includes  $70811 \pm 267$  (stat.) ( $20036 \pm 145$  (stat.)) IBD candidates and  $20534 \pm 16$  (stat.) ( $1436 \pm 4$  (stat.)) accidental coincidences measured by a 10 ms wide off-time window, resulting in  $50277 \pm 267$  (stat.) ( $18600 \pm 145$  (stat.)) correlated events. A bin-wise subtraction of reactor-on and reactor-off correlated candidates yields the energy spectrum of  $31678 \pm 304$  (stat.) detected  $\bar{\nu}_e$  shown in Fig. 3. A correlated event signal-to-background ratio of 1.7:1 is observed. The correlation of background rate with local atmospheric pressure is characterized during reactor-off periods and results in a correction factor of  $0.991 \pm 0.004$  based on the average pressure during reactor-on periods [33, 34].

After all cuts are applied, the dominant backgrounds are produced by cosmogenic activity. The IBD-like background spectrum is comprised of three components. The 4.4 MeV peak and continuum are from fast neutron primary inelastic scattering on carbon and other material in the detector volume. The observed 2.2 MeV peak is from multiple neutron events where the first captures on hydrogen. These are produced by a combination of muon and fast neutron primaries.

Multiple validations of the energy reconstruction, background subtraction methods, and the PG4 detector model have been performed. This is particularly important given the segmented nature of the PROSPECT detector, the presence of inactive volume, and the prominent features present in the near-surface background spectrum. Subdivisions of the dataset based on acquisition time and event position are used as the primary validation method. Comparison of reactor-off data split into two time periods (Fig. 4) indicates consistency in both rate and shape, validating the atmospheric pressure scaling and energy reconstruction stability. Similarly, the reactor-on and off data are split into two independent data sets and the full analysis is performed on each portion separately. No difference is observed between these two subdivisions. Several

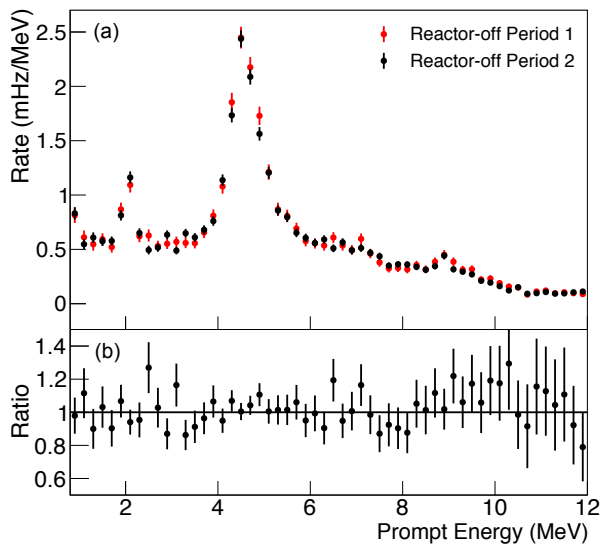


FIG. 4. The reactor-off data is split into two time periods. (a) Spectra of IBD candidate events (with statistical errors only). (b) Ratio between periods. The observed consistency between these periods demonstrates the stability of cosmogenic IBD candidates after accounting for atmospheric conditions.

division schemes based on event position were also examined by splitting the detector in quadrants, near and far halves from the reactor, and inner and outer segment regions. Consistency was found between the spectra independently measured in the first two cases, while differences in relative spectral shape due to greater energy leakage in outer segments predicted by the detector PG4 model were successfully reproduced in the latter case. A mean IBD prompt event multiplicity of 2.66 segments is found in both the predicted and observed IBD topology.

A  $\chi^2$  test is employed to quantify the comparison of models to the experimental data:

$$\chi_{min}^2 = \Delta^T V^{-1} \Delta, \quad (1)$$

where  $V$  is the full covariance matrix and  $\Delta$  is the difference between the measured and predicted spectrum. Simulations are performed separately varying detector parameters, including energy scale, inactive material, energy thresholds, and fiducialization, according to experimental uncertainties. Covariance matrices are generated for each parameter to capture both correlated and uncorrelated uncertainties. The observed variation between the two reactor-off periods is used to construct a background subtraction covariance matrix. An additional background subtraction uncertainty is included to account for the independent variation of the muon-induced and fast-neutron induced background components. Finally, the uncorrelated statistical uncertainties from the reactor-on and off periods are used to build the full covariance matrix [32].

The Huber  $^{235}\text{U}$  antineutrino spectrum [8] is adjusted for the IBD cross-section and passed through the PROSPECT detector response matrix to produce a prompt energy prediction. The three-neutrino framework is assumed and no correction is

made for possible spectral distortions from sterile neutrino oscillations. Corrections for non-equilibrium isotopes produced during the 24-day reactor cycle are added according to the procedure in Ref. [7]. A detailed model of the core is used to estimate the  $\bar{\nu}_e$  flux generated via beta decay of  $^{28}\text{Al}$  nuclei produced by neutron capture on the fuel cladding [35]. Integrated over the full spectrum, each of these corrections amount to less than 1% of the total  $\bar{\nu}_e$  flux. A shape-only comparison, shown in Fig. 5, is achieved by normalizing the prediction to the number of observed events. A high  $\chi^2/\text{ndf}$  is observed (51.6/31) indicating marginal agreement between the model and the experimental data.

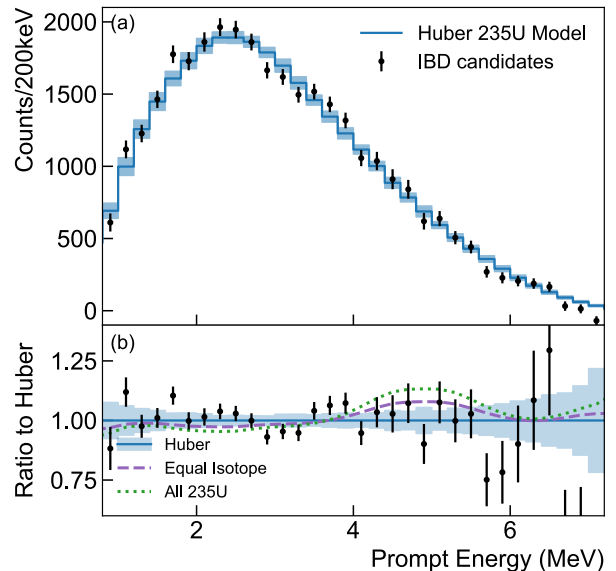


FIG. 5. (a): The measured prompt energy spectrum of inverse beta decay events compared to prediction based on the Huber  $^{235}\text{U}$  model. The error bars include only statistical uncertainties, while the shaded band includes detector and model uncertainties. (b): Ratio to the Huber model of the measured data and two ad-hoc models used for the frequentist  $\Delta\chi^2$  comparison.

Spectral measurements at LEU reactors have observed discrepancies relative to their model predictions, particularly in the 4-6 MeV region. With an average fission fraction of  $\sim 55\%$ ,  $^{235}\text{U}$  is the dominant fissile isotope present in LEU reactors. To compare the PROSPECT measured HEU spectrum with those from LEU reactors, hypothetical models based on different interpretations of these LEU measurements are constructed. First, the observed discrepancies could be caused by mis-modeling of  $\bar{\nu}_e$  spectra from isotopes other than  $^{235}\text{U}$ , leaving the  $^{235}\text{U}$  portion of the spectrum well-modeled by the Huber beta-conversion prediction [17]. Second, there could be a common mis-modelling of all  $\bar{\nu}_e$  spectra (the ‘‘Equal Isotope’’ hypothesis). Finally, the discrepancies could be entirely due to errors in the  $^{235}\text{U}$   $\bar{\nu}_e$  prediction (the ‘‘All  $^{235}\text{U}$ ’’ hypothesis). Ad-hoc models are constructed for the latter two hypotheses by applying modifications to the full Huber  $^{235}\text{U}$  spectrum derived from the observed ratio between Daya Bay’s

data and reported LEU prediction [36]. The resulting hypotheses' prompt energy predictions are shown in the lower panel of Fig. 5 as a ratio with respect to the Huber-predicted prompt spectrum. To ensure an equal comparison between the models, we have used the same uncertainties from the Huber model for the modified predictions. The ad-hoc models have a  $\chi^2/\text{ndf}$  of 52.1/31 and 58.9/31 for the "Equal Isotope" and "All  $^{235}\text{U}$ ," respectively.

To quantify the comparison between Huber and the ad-hoc models, we employ a frequentist approach. Using the full covariance matrix,  $10^6$  toy-experiments are generated for each of the three hypotheses. A probability distribution function (PDF) is formed from the  $\Delta\chi^2$  values for each toy experiment between the three models. The observed experimental  $\Delta\chi^2$  values are compared to their respective PDFs to determine quantitative preference of the observation for a particular model. We find that the 7.3 and 6.8  $\Delta\chi^2$  of the "All  $^{235}\text{U}$ " hypothesis with respect to the Huber and Equal Isotope models correspond to p-values of 0.0019 and 0.0016, indicating  $\sim 3\sigma$  disfavoring of the "All  $^{235}\text{U}$ " hypothesis. No preference is observed between the Equal Isotope and Huber hypotheses.

With over 31000 IBD interactions, PROSPECT has produced the highest statistics measurement of the  $^{235}\text{U}$  antineutrino energy spectrum to date. The Huber model reproduces the general features of the measured spectrum, but exhibits a large  $\chi^2$  with respect to it. This  $\chi^2$  is not improved by modifications derived from recent measurements at LEU reactors. The hypothesis that the LEU spectral discrepancy is entirely caused by  $^{235}\text{U}$  is disfavored at  $\sim 3\sigma$ . This is a statistics-limited measurement and is expected to improve as more data are collected.

This material is based upon work supported by the following sources: US Department of Energy (DOE) Office of Science, Office of High Energy Physics under Award No. DE-SC0016357 and DE-SC0017660 to Yale University, under Award No. DE-SC0017815 to Drexel University, under Award No. DE-SC0008347 to Illinois Institute of Technology, under Award No. DE-SC0016060 to Temple University, under Contract No. DE-SC0012704 to Brookhaven National Laboratory, and under Work Proposal Number SCW1504 to Lawrence Livermore National Laboratory. This work was performed under the auspices of the U.S. Department of Energy by Lawrence Livermore National Laboratory under Contract DE-AC52-07NA27344 and by Oak Ridge National Laboratory under Contract DE-AC05-00OR22725. Additional funding for the experiment was provided by the Heising-Simons Foundation under Award No. #2016-117 to Yale University.

J.G. is supported through the NSF Graduate Research Fellowship Program and A.C. performed work under appointment to the Nuclear Nonproliferation International Safeguards Fellowship Program sponsored by the National Nuclear Security Administrations Office of International Nuclear Safeguards (NA-241). This work was also supported by the Canada First Research Excellence Fund (CFREF), and the Natural Sciences and Engineering Research Council of Canada (NSERC) Discovery program under grant #RGPIN-

418579, and Province of Ontario.

We further acknowledge support from Yale University, the Illinois Institute of Technology, Temple University, Brookhaven National Laboratory, the Lawrence Livermore National Laboratory LDRD program, the National Institute of Standards and Technology, and Oak Ridge National Laboratory. We gratefully acknowledge the support and hospitality of the High Flux Isotope Reactor and Oak Ridge National Laboratory, managed by UT-Battelle for the U.S. Department of Energy.

---

\* Also at: Department of Chemistry and Chemical Technology, Bronx Community College, Bronx, NY, USA.

† Also at: Yale Center for Research Computing, Yale University, New Haven CT 06520

‡ prospect.collaboration@gmail.com

- [1] C. L. Cowan, F. Reines, F. B. Harrison, H. W. Kruse, and A. D. McGuire, *Science* **124**, 103 (1956).
- [2] K. Eguchi *et al.* (KamLAND), *Phys. Rev. Lett.* **90**, 021802 (2003), arXiv:hep-ex/0212021 [hep-ex].
- [3] T. Araki *et al.*, *Nature* **436**, 499 (2005).
- [4] F. P. An *et al.* (Daya Bay), *Phys. Rev. Lett.* **108**, 171803 (2012), arXiv:1203.1669 [hep-ex].
- [5] J. K. Ahn *et al.* (RENO), *Phys. Rev. Lett.* **108**, 191802 (2012), arXiv:1204.0626 [hep-ex].
- [6] Y. Abe *et al.* (Double Chooz), *Phys. Rev. Lett.* **108**, 131801 (2012), arXiv:1112.6353 [hep-ex].
- [7] T. A. Mueller *et al.*, *Phys. Rev.* **C83**, 054615 (2011), arXiv:1101.2663 [hep-ex].
- [8] P. Huber, *Phys. Rev.* **C84**, 024617 (2011), [Erratum: *Phys. Rev.* **C85**, 029901(2012)], arXiv:1106.0687 [hep-ph].
- [9] F. P. An *et al.* (Daya Bay), *Phys. Rev. Lett.* **116**, 061801 (2016), [Erratum: *Phys. Rev. Lett.* **118**, no.9, 099902(2017)], arXiv:1508.04233 [hep-ex].
- [10] Y. Abe *et al.* (Double Chooz), *JHEP* **10**, 086 (2014), [Erratum: *JHEP* **02**, 074(2015)], arXiv:1406.7763 [hep-ex].
- [11] S.-H. Seo (RENO), *Proceedings, 26th International Conference on Neutrino Physics and Astrophysics (Neutrino 2014): Boston, Massachusetts, United States, June 2-7, 2014*, AIP Conf. Proc. **1666**, 080002 (2015), arXiv:1410.7987 [hep-ex].
- [12] Y. Ko *et al.* (NEOS), *Phys. Rev. Lett.* **118**, 121802 (2017), arXiv:1610.05134 [hep-ex].
- [13] F. P. An *et al.* (Daya Bay), *Phys. Rev. Lett.* **118**, 251801 (2017), arXiv:1704.01082 [hep-ex].
- [14] G. Bak *et al.* (RENO), (2018), arXiv:1806.00574 [hep-ex].
- [15] A. C. Hayes, J. L. Friar, G. T. Garvey, G. Jungman, and G. Jonkmans, *Phys. Rev. Lett.* **112**, 202501 (2014), arXiv:1309.4146 [nucl-th].
- [16] D. A. Dwyer and T. J. Langford, *Phys. Rev. Lett.* **114**, 012502 (2015), arXiv:1407.1281 [nucl-ex].
- [17] A. C. Hayes, J. L. Friar, G. T. Garvey, D. Ibeling, G. Jungman, T. Kawano, and R. W. Mills, *Phys. Rev.* **D92**, 033015 (2015), arXiv:1506.00583 [nucl-th].
- [18] X. B. Wang, J. L. Friar, and A. C. Hayes, *Phys. Rev.* **C94**, 034314 (2016), arXiv:1607.02149 [nucl-th].
- [19] X. B. Wang and A. C. Hayes, *Phys. Rev.* **C95**, 064313 (2017), arXiv:1702.07520 [nucl-th].
- [20] A. Sonzogni, E. McCutchan, and A. Hayes, *Phys. Rev. Lett.* **119**, 112501 (2017).

- [21] Y. Gebre, B. R. Littlejohn, and P. T. Surukuchi, *Phys. Rev.* **D97**, 013003 (2018), arXiv:1709.10051 [hep-ph].
- [22] B. R. Littlejohn, A. Conant, D. A. Dwyer, A. Erickson, I. Gustafson, and K. Hermanek, *Phys. Rev.* **D97**, 073007 (2018), arXiv:1803.01787 [nucl-th].
- [23] G. Mention, M. Fechner, T. Lasserre, T. A. Mueller, D. Lhuillier, M. Cribier, and A. Letourneau, *Phys. Rev.* **D83**, 073006 (2011), arXiv:1101.2755 [hep-ex].
- [24] C. Giunti, X. P. Ji, M. Laveder, Y. F. Li, and B. R. Littlejohn, *JHEP* **10**, 143 (2017), arXiv:1708.01133 [hep-ph].
- [25] N. Allemandou *et al.* (STEREO), *JINST* **13**, P07009 (2018), arXiv:1804.09052 [physics.ins-det].
- [26] Y. Abreu *et al.* (SoLid), *JINST* **12**, P04024 (2017), arXiv:1703.01683 [physics.ins-det].
- [27] J. Ashenfelter *et al.* (PROSPECT), (2018), arXiv:1808.00097 [physics.ins-det].
- [28] J. Ashenfelter *et al.* (PROSPECT), *Phys. Rev. Lett.* **121**, 251802 (2018), arXiv:1806.02784 [hep-ex].
- [29] H. Kwon, F. Boehm, A. A. Hahn, H. E. Henrikson, J. L. Vuilleumier, J. F. Cavaignac, D. H. Koang, B. Vignon, F. Von Feilitzsch, and R. L. Mossbauer, *Phys. Rev.* **D24**, 1097 (1981).
- [30] J. Allison *et al.*, *Nucl. Instrum. Meth.* **A835**, 186 (2016).
- [31] J. B. Birks, *The Theory and practice of scintillation counting* (1964).
- [32] Full detector response matrix, covariance matrix, and data points can be found in Supplemental Material.
- [33] J. A. Lockwood and H. E. Yingt, *Phys. Rev.* **104**, 1718 (1956).
- [34] “Oak Ridge Reservation Meteorology,” <https://metweb.ornl.gov>, Accessed: 2018-11-02.
- [35] J. Swartout, A. Boch, T. Cole, R. Cheverton, G. Adamson, and C. Winters, *The Oak Ridge High Flux Isotope Reactor*, Tech. Rep. 4042265 (Oak Ridge National Laboratory, 1964).
- [36] F. P. An *et al.* (Daya Bay), *Chin. Phys.* **C41**, 013002 (2017), arXiv:1607.05378 [hep-ex].